**THE EUROPEAN
PHYSICAL JOURNAL B**

Regular Article

Efficient and accurate modeling of electron photoemission in nanostructures with TDDFT

Philipp Wopperer[1,a], Umberto De Giovannini[1,2], and Angel Rubio[1,3]

[1] Nano-Bio Spectroscopy Group and ETSF, Universidad del País Vasco, CFM CSIC-UPV/EHU, 20018 San Sebastián, Spain
[2] Dipartimento di Fisica e Chimica, Università degli Studi di Palermo, Via Archirafi 36, 90123 Palerme, Italy
[3] Max Planck Institute for the Structure and Dynamics of Matter and Center for Free-Electron Laser Science, Luruper Chaussee 149, 22761 Hamburg, Germany

Abstract. We derive and extend the time-dependent surface-flux method introduced in [L. Tao, A. Scrinzi, New J. Phys. **14**, 013021 (2012)] within a time-dependent density-functional theory (TDDFT) formalism and use it to calculate photoelectron spectra and angular distributions of atoms and molecules when excited by laser pulses. We present other, existing computational TDDFT methods that are suitable for the calculation of electron emission in compact spatial regions, and compare their results. We illustrate the performance of the new method by simulating strong-field ionization of C_{60} fullerene and discuss final state effects in the orbital reconstruction of planar organic molecules.

1 Introduction

When physical systems such as atoms, molecules, clusters, or nano-objects are exposed to an appropriately tuned radiation field there is a non-negligible chance of ionization. Strictly speaking, electron photoemission takes place whenever the exciting field is capable to induce a bound-to-continuum transition and results in electrons escaping with a given kinetic energy and from a given direction. Depending on the characteristics of the radiation, the target system, time and energy scales, there exist many mechanisms that contribute to emit electrons and correspondingly many ways to categorize them: for example, sequential (Fano resonances, Auger decay, autoionization/thermionic emission) and non-sequential processes, single and double ionization, single- and multiphoton ionization, above-threshold ionization, etc. Associated with each of these mechanisms there is as much spectroscopic information to be extracted. In particular, knowledge about the ionization dynamics and on the parent system can be gained from differential observables of the electron yield. For instance, the electron photoemission probability as a function of the kinetic energy – the photoelectron spectrum (PES) – can give insight into electronic energy levels, while the photoelectron angular distribution (PAD) carries spatial information on ionic positions or directly on the electronic configurations.

If we focus on the ionization mechanism as a function of the external field parameters, we can distinguish among different regimes. A common classification of the predominant ionization regimes is according to the Keldysh parameter [1], originally defined for the hydrogen atom. This parameter is given by $\gamma = \sqrt{E_{IP}/(2U_p)}$ with E_{IP} being the ionization potential of the system, $U_p = I/(4\omega^2)$ the ponderomotive energy (i.e., the averaged quiver energy in atomic units), I the intensity of the irradiating light, and ω the frequency. For $\omega \ll E_{IP}$, one distinguishes two ionization regimes according to the Keldysh parameter: the perturbative or nonlinear multiphoton ionization regime (MPI) [2] which is associated with $\gamma > 1$ and the strong-field ionization regime with $\gamma < 1$.

In the multiphoton regime, the laser action results in a vertical excitation of a bound electron into the continuum by absorption of several photons. Nevertheless, weak and moderate lasers can promote electrons also far into the continuum by absorption of multiple photons above the ionization threshold. This non-perturbative process is called above-threshold ionization (ATI) [3] and yields to spectra which decay exponentially in energy and that are characterized by a series of peaks separated by ω.

In the past decade, research in the photoelectron spectroscopy of finite systems has focused predominantly on the strong-field regime which is characterized by the onset of optical field ionization. At sufficiently high field strengths, the barrier of the binding Coulomb potential is suppressed which results in a tunneling current that follows adiabatically the variation of the laser field [4]. Above-threshold ionization still prevails in this regime, however, it is more suitably explained as interferences between coherent photoelectron wavepackets emitted at different times within the laser cycle.

Photoelectron spectra and angular distributions in the strong-field regime are particularly rich in information on ionization dynamics since field-driven rescattering

[a] e-mail: philipp.wopperer@ehu.es

is involved. This process was described by a classical three-step model, also called simpleman's model [5,6] and was later extended to a quantum description (strong-field approximation) [7] using the Keldysh-Faisal-Reiss approximation [1,8,9]. According to the three-step model the electron is first released by tunnel ionization. The tunneled electron is then accelerated in the laser field where it acquires a kinetic energy. Depending on the release time, electrons either leave the parent ion directly or are driven back towards the parent ion once the laser field changes its sign [10]. Applications of the field-driven rescattering process are manifold. For instance, rescattering coherent electron wavepackets can be used to self-interrogate the parent molecular structure. This phenomenon is exploited for laser-induced electron diffraction (LIED) [11,12] to image molecular structures. Rescattering and direct photoelectron wavepackets can also interfere coherently which allows to study holographic pattern in photoemission spectra and angular distributions [13]. Nevertheless, reading recollision induced diffraction images can become a complex task as several processes compete on similar time and energy scales [14].

Concerning materials and investigated species in photoemission experiments, research has extended to larger and denser systems in the previous years. Quite recently, signatures of strong-field physics were found by experiments in metallic surfaces [15] and nanostructures [16], clusters [17], and dielectric nanospheres [18]. For instance, the exploration of photoionization processes in metal nanotips is currently a strongly evolving field of research. The combination of femtosecond laser pulses and a sharp metal tip is considered as a laser-driven ultrafast electron emitter on the nanometer scale with prospective applications as electron source in electron microscopy, electron diffraction and for free electron lasers, as an extremely sensitive carrier-envelope phase sensor, or as generators of high-harmonic radiation [19–22].

Calculation of PADs from the perturbative to the strong-field regime, and accurate modeling of photoemission experiments on a broad range of materials at the same time, can only be achieved by a comprehensive approach. In general, the interaction between electrons in an atom or a molecule and a laser field is difficult to treat theoretically, and several approximations are usually employed. For one-electron systems, PES and PAD can be calculated exactly bydirectly solving the time-dependent Schrödinger equation (TDSE). The most straightforward way is by projecting the wavefunction obtained from the TDSE at the end of the pulse onto continuum states [23]. Another approach where the calculation of the continuum eigenstates is avoided, is the resolvent technique [24]. Both methods need to propagate the wavefunction until the end of the pulse in a large space domain in order to obtain the correct distribution of the ejected electrons. For simple cases this problem can be overcome by the use of spherical coordinates. Also geometrical splitting techniques [25–27] turn out to be very useful to reduce computational cost.

For more than two electrons, the exact solution of the TDSE in three dimensions is unfeasible and basically all ab-initio calculations for multielectron systems are performed under the single-active electron (SAE) approximation. In the SAE only one electron interacts with the external field while the other electrons are frozen. This approximation was successfully employed in several photoemission studies for atoms and molecules in strong laser fields [28–30]. Besides the TDSE, Floquet theory [31,32], the strong-field approximation [33,34] and semi-classical methods [35–38] based on ionization rates [39] are used in the strong-field regime. For weak lasers, plane wave methods [40], the independent atomic center approximation [41] and (multiphoton) perturbation theory [42–44] are usually employed. However, such approaches reproduce dynamics only qualitatively, and their failure to describe multielectron (correlation) effects and their often oversimplified assumptions for the continuum state call for better schemes.

The inclusion of exchange-correlation effects for a system of many interacting electrons can be achieved within time-dependent density-functional theory (TDDFT) [45,46]. Computations of electronic excitations for systems with up to a few hundred atoms are currently most widely carried out employing this method. TDDFT offers a reasonable trade-off between accuracy and computational cost, where other, more accurate, methods [47,48] would not be feasible. In spite of transferring all the many-body problems into an unknown exchange-correlation functional, the calculation of PES and PAD in TDDFT is not straightforward. While the total ionization yield can be calculated directly, differential quantities cannot be expressed in terms of the electron density. Methods based on TDDFT, therefore, assume that PES and PAD can be directly obtained from the time-dependent Kohn-Sham orbitals. Nevertheless, a close correspondence between spectroscopic data and Kohn-Sham orbitals exists when using self-interaction-free exchange and correlation functionals [49].

For TDDFT there are only two methods to compute PES and PAD that can be formulated in finite volumes and that do not require to explicitly calculate continuum states [50]: the sampling point method (SPM) [51,52] and the mask method (MM) [53]. Both of them were extensively and successfully used for the calculation of photoelectron spectra of atoms, molecules, and clusters [54], model systems for nano-tips [55], and for various experimental setups from time-resolved (pump-probe) spectroscopy [56,57] to strong-field ionization of atoms exposed the X-rays [58]. However, both methods present limitations in practical applications. For instance, MM becomes demanding to converge for low kinetic energies ($E \lesssim 1$ eV). This is because MM requires Fourier transforms of the wavefunctions. Thus, small energy steps and consequently small momenta are associated with large spatial dimension that become increasingly large as we decrease the step. Furthermore, the use of Fourier transforms prevents efficient parallelization in spatial domains which in turns limits the size of the largest simulation box to a single computational node memory. On the other end, SPM is less limited from the computational stand point,

but is unreliable especially in the strong-field regime. This is due to the strong assumptions that it needs which are difficult to assess and in turn require comparatively large simulations boxes to appropriately converge.

A promising alternative method was proposed in references [59,60], and a preliminary version of the same method in reference [61] – the time-dependent surface flux method (t–SURFF). t–SURFF has been so far employed only for few-electron systems either with TDSE [59,60,62] or in combination with multiconfigurational time-dependent Hartree-Fock [61]. In this paper, we extend this method for the first time to TDDFT. In Section 2, we present the theory alongside the sampling point and mask methods to illustrate differences and common traits and proceed with a real world comparison on a characteristic set of examples in Section 3. For the sake of simplicity, we restrict ourselves here and following to spin-unpolarized many-electron systems. Nevertheless, all expressions and calculations can be trivially extended to include spin polarization.

Atomic units will be used throughout ($m_e = e = \hbar = 1$) unless otherwise indicated.

2 Theory

2.1 Space partitioning and momentum distribution

Below, we formally present the theoretical framework and assumptions that are common to all the three methods detailed in the next sections. In this paper, we describe the many-body electron dynamics at the level of TDDFT [45,46]. In this context, the electronic density of a many-body system

$$\rho(\mathbf{r}, t) = \sum_{i=1}^{N} |\varphi_i(\mathbf{r}; t)|^2,$$

is obtained from an auxiliary one – the Kohn-Sham (KS) system – of non-interacting fermions which wavefunction is represented by a single Slater determinant $\Psi(\mathbf{r}; t)$ composed of N orbitals $\varphi_i(\mathbf{r}; t)$. These orbitals satisfy the time-dependent KS equations

$$\imath \partial_t \varphi_i(\mathbf{r}; t) = \hat{H}_{\mathrm{KS}} \, \varphi_i(\mathbf{r}; t), \qquad (1)$$

with the time-dependent KS Hamiltonian

$$\hat{H}_{\mathrm{KS}}[\rho](\mathbf{r}; t) = -\frac{\Delta}{2} + V_{\mathrm{KS}}[\rho](\mathbf{r}; t), \qquad (2)$$

and the time-dependent KS potential

$$V_{\mathrm{KS}}[\rho](\mathbf{r}; t) = V_{\mathrm{ext}}(\mathbf{r}; t) + \int d^3 r' \frac{\rho(\mathbf{r}'; t)}{|\mathbf{r} - \mathbf{r}'|} + V_{\mathrm{xc}}[\rho](\mathbf{r}; t), \quad (3)$$

composed by the external field of the ions and the laser field, the classical Hartree and the exchange and correlation (xc) potential. Once the time-dependent density is
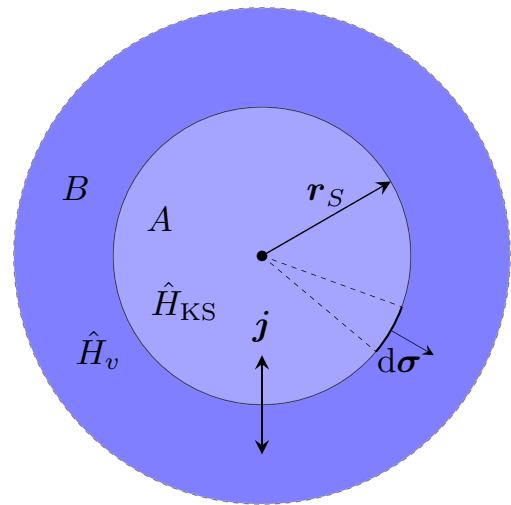

Fig. 1. Schematic description of space partitioning in the surface flux, sampling point, and mask methods. A surface S (here chosen as spherical) separates the space into region A which is described by TDDFT and the Volkov propagation region B.

obtained by solving these equations, it is in principle possible to access any kind of observable provided it is expressed as a functional of $\rho(\mathbf{r}, t)$.

The momentum probability distribution of emitted electrons $P(\mathbf{k})$, i.e. the probability to measure an electron with momentum $\mathbf{k}$ at a detector positioned far away from a target system, is the observable we aim to describe. In this work, we focus on the formulations that can be applied to real-space implementations and that require the knowledge of the wavefunction in a limited volume. All these approaches are resting on two principal assumptions.

The first assumption is that the dynamics of ionization can be accurately described by two different Hamiltonians localized in adjacent spatial regions A and B separated by a surface S as in Figure 1 – we here choose a spherical surface of radius r_S, but the shape can be general. More specifically, we assume that in A the electrons can be described with the KS Hamiltonian of equation (2) while in B they follow the exactly solvable Volkov Hamiltonian

$$\hat{H}^B(t) = \hat{H}_v(t) = \frac{1}{2} \left[-\imath \nabla - \frac{\mathbf{A}(t)}{c} \right]^2 \qquad (4)$$

governing the time evolution of free electrons in an external field $\mathbf{A}(t)$. This means that the total time-dependent Hamiltonian $\hat{H}(\mathbf{r}; t)$ describing our system can be expressed as a combination of these two spatially localized Hamitonians,

$$\hat{H}(\mathbf{r}; t) = \begin{cases} \hat{H}_A(\mathbf{r}; t) = \hat{H}_{\mathrm{KS}}(\mathbf{r}; t) & \mathbf{r} \in A \\ \hat{H}_B(\mathbf{r}; t) = \hat{H}_v(\mathbf{r}; t) & \mathbf{r} \in B, \end{cases} \qquad (5)$$

and that electrons in B can be safely described as free, independent particles. The quality of such an assumption is limited by the error in the truncation of the tail of the Coulomb potential and ultimately depends on the position of S relative to the target system. While this is exact

in the proximity of the detector – at an infinite distance – and certainly bad in the vicinity of the system – where electrons are strongly interacting with each other and with the external potential – its range of applicability in many relevant situations is quite large. In practice, however, one has to converge the final results with respect to S.

Under the assumption that the space partitioning is a good approximation, we can represent the wavefunction in B with a KS Slater determinant $\Psi^B(\mathbf{r}; t)$ yet expand each orbital $\varphi_i^B(\mathbf{r}; t)$ on Volkov waves as follows

$$\varphi_i^B(\mathbf{r}; t) = \int d^3 k\, b_i(\mathbf{k}) \chi_{\mathbf{k}}(\mathbf{r}; t), \tag{6}$$

where

$$\chi_{\mathbf{k}}(\mathbf{r}; t) = (2\pi)^{-3/2} e^{-\imath \Phi(\mathbf{k}; t)} e^{\imath \mathbf{k}\mathbf{r}}, \tag{7}$$

with

$$\Phi(\mathbf{k}; t) = \frac{1}{2} \int_0^t d\tau \left[\mathbf{k} - \frac{\mathbf{A}(\tau)}{c}\right]^2 \tag{8}$$

are the exact solutions of the time-dependent Schrödinger equation for the Volkov Hamiltonian in equation (4), $\Phi(\mathbf{k}; t)$ is the Volkov phase and $b_i(\mathbf{k})$ is the spectral amplitude of the ith KS orbital. Volkov waves are essentially plane waves with an additional time-dependent phase.

The second assumption is that in the long time limit, for $t \geq T$, bound and ionized electronic wavefunctions are well localized in A and B, respectively. In other words, we demand that the total density is given by $\rho(\mathbf{r}; T) = \rho^A + \rho^B$ with

$$\rho^A = \sum_{i=1}^N |\varphi_i^A(\mathbf{r}; T)|^2, \qquad \rho^B = \sum_{i=1}^N |\varphi_i^B(\mathbf{r}; T)|^2, \tag{9}$$

and with $\varphi_i^A(\mathbf{r}; T)$ $(\varphi_i^B(\mathbf{r}; T))$ being the ith KS orbital localized in A (B) at time T. This is exact for $T \to \infty$, while for finite values of T one has to propagate for a time long enough such that slowest escaping electrons have reached region B.

Under the former assumptions the total number of electrons escaped from A at time T, which is precisely the integral of the total density in B, can be expressed as

$$N_{\text{esc}} = \int_B d^3 r\, \rho(\mathbf{r}; T) = \int d^3 r\, \rho^B(\mathbf{r}; T)$$
$$= \sum_{i=1}^N \int d^3 k\, |b_i(\mathbf{k})|^2 \tag{10}$$

where we used equation (6) to obtain the rightmost expression. Since the momentum distribution $P(\mathbf{k})$ is the differential probability associated with the total number of escaped electrons we can use the completeness of Volkov

functions to invert equation (6) and obtain that

$$P(\mathbf{k}) = \frac{d^3 N_{\text{esc}}}{d^3 k} = \sum_{i=1}^N |b_i(\mathbf{k})|^2$$
$$= \sum_{i=1}^N \left| \langle \chi_{\mathbf{k}}(T) | \varphi_i^B(T) \rangle \right|^2. \tag{11}$$

From this equation it is apparent how $P(\mathbf{k})$ connects with the spectral amplitude $b_i(\mathbf{k})$ of the scattering orbitals expanded on Volkov waves. Less resolved quantities, like the energy-resolved photoelectron probability $P(E = k^2/2)$, can be obtained from $P(\mathbf{k})$ by direct integration.

The three methods which we describe in the next sections, essentially provide different approaches to obtain $b_i(\mathbf{k})$ from the knowledge of the KS orbitals in A only. Our aim is to have an expression for $b_i(\mathbf{k})$ which can be efficiently implemented in a real space three dimensional representation, that is accurate from linear to strong-field regimes and with an energy resolution comparable to experiment ($\Delta E \sim 0.05$ eV). As we will show in the following, the SPM is straightforward to implement efficiently and provides a large flexibility in reciprocal space. However, it is unreliable in the mid- to strong-field regimes where it requires the use of unpractically large simulation boxes to properly converge under its working assumptions. MM, in contrast, yields reliable and precise results in all regimes, however, a computationally efficient implementation is more involved as Fourier transforms are needed. Moreover, when using this method the reciprocal space grid is constrained by the choice of the real-space one and spectra at low kinetic energies are difficult to retrieve. t–SURFF can be derived in a TDDFT formalism without any additional assumptions. The grid in momentum space can be chosen arbitrarily which allows the calculation of PES and PAD up to high precision and resolution. Furthermore, by introducing an additional parameter (the angular momentum cut-off $L_{\max}$) the method can be efficiently implemented in three dimensions.

2.2 Sampling point method

The sampling point method (SPM) is the oldest and least accurate amongst the methods we discuss in this work [51]. It was first presented without formal theoretical derivation and justified only on the basis of its results on practical calculations. We hereby present a derivation with particular attention to the conditions under which it is supposed to work reliably.

The SPM is based on the idea that $P(\mathbf{k})$ can be calculated by the simple knowledge of the time dependence of each orbital sampled only at a single point $\mathbf{r}_S$ of the surface S in Figure 1. Besides the assumptions discussed in the previous section, it rests on the additional conditions that (i) $\mathbf{r}_S$ is positioned at a sufficiently large distance such that the ionized wavepackets arrive when the laser pulse has been switched off (for $t \geq T_{\text{pulse}}$) and (ii) with a final momentum directed along $\mathbf{r}_S$, i.e., $\mathbf{k} = k\mathbf{e}_{\mathbf{r}_S}$.

Under these conditions we can drop the field $\mathbf{A}(t)$ in the Volkov phase which then describes free particles, and explicitly write the expansion of equation (6) as

$$\varphi_i^B(\mathbf{r}_S; t) = (2\pi)^{-3/2} \int d\mathbf{k}\, b_i(k, \Omega_{\mathbf{r}_S}) e^{\imath k r_S - \imath k^2 t/2}, \quad (12)$$

where we express the momentum vector in spherical coordinates $\mathbf{k} = (k, \Omega_{\mathbf{r}_S})$ to stress the form enforced to the final momentum by condition (ii). A Fourier transform in the time domain is then sufficient to impose the free particle dispersion relation, $E = k^2/2$, and extract the Volkov amplitudes with the following result

$$\tilde{\varphi}_i^B(\mathbf{r}_S; E) = \frac{1}{\sqrt{2\pi}} \int dt\, e^{\imath E t} \varphi_i^B(\mathbf{r}_S; t)$$
$$= \frac{e^{\imath \sqrt{2E} r_S}}{\sqrt{2E(2\pi)^3}} b_i(\sqrt{2E}, \Omega_{\mathbf{r}_S}). \quad (13)$$

To obtain the above relation we used the time condition (i) and the Dirac delta $\delta(E - k^2/2)$ resulting from the time integral to simplify equation (12). At this point the momentum distribution probability can be straightforwardly obtained from equation (11) as

$$P\left(\mathbf{k} = (\sqrt{2E}, \Omega_{\mathbf{r}_S})\right) = 2E(2\pi)^3 \sum_{i=1}^{N} \left|\tilde{\varphi}_i^B(\mathbf{r}_S; E)\right|^2, \quad (14)$$

where we explicitly inverted the dispersion relation to obtain the momentum magnitude $k = \sqrt{2E}$. This implies that k is always positive and therefore we must further impose that (iii) at the sampling point, the electrons are strictly outgoing.

The SPM working conditions are asymptotically valid for $\mathbf{r}_S$ positioned at an infinitely large distance from the system, but quickly degrade as we move closer. The most stringent condition is the time constraint (i) since it directly forces $\mathbf{r}_S$ to be positioned at a distance that proportionally grows with the laser switch-off time T_{pulse}.

A simple way to overcome this limitation was proposed in reference [52]. It substantially reduces to keeping the full Volkov phase, including the field, in the expansion of equation (6) and to compensate it in the Fourier time integral. The Fourier exponent iEt in equation (13) is thus substituted with the Volkov phase $i\Phi(\mathbf{k}; t)$ evaluated at $\mathbf{k} = \sqrt{2E} \mathbf{e}_{\mathbf{r}_S}$,

$$\tilde{\xi}_i^B(\mathbf{r}_S; E) = \frac{1}{\sqrt{2\pi}} \int dt\, e^{\imath \Phi(\sqrt{2E} \mathbf{e}_{\mathbf{r}_S}; t)} \varphi_i^B(\mathbf{r}_S; t). \quad (15)$$

The photoelectron momentum distribution is then obtained by simply replacing $\tilde{\varphi}_i^B(\mathbf{r}_S; E)$ with $\tilde{\xi}_i^B(\mathbf{r}_S; E)$ in equation (14). Owing to the presence of the Volkov phase in the time integral this variant goes under the name of phase-augmented sampling point method (PA-SPM).

Even though this approach is superior to the simple SPM, it is still limited by conditions (ii) and (iii). The validity of these conditions is difficult to assess in practical calculations since it strongly depends on the electron dynamics induced by the external field and can only be taken under control by converging the final results with respect to the position of $\mathbf{r}_S$.

2.3 Surface flux method

In contrast to the SPM, the time-dependent surface flux method (t–SURFF) [59–61] makes no further assumption besides the ones discussed in Section 2.1. Thus, for instance, it can handle situations where electrons are driven by the laser field back towards the emission site like in the backscattering regime. We here describe a derivation alternative to the one present in the literature. Our derivation is based on the flux of the current-density operator through S (see the scheme of Fig. 1) that is suitable for TDDFT.

Owing to the space and Hamiltonian partitioning explained in Section 2.1, we can describe the electronic wavefunctions with both $\Psi_A(\mathbf{r}; t)$ and $\Psi_B(\mathbf{r}; t)$ on the surface S that separates region A and B. Using the continuity equation we thus express the total number of escaped electron N_{esc} at time T in terms of the flux integral

$$N_{\text{esc}} = \int_0^T dt \int_B d^3r\, \frac{d\rho(\mathbf{r}; t)}{dt} = -\int_0^T dt \int_S d\boldsymbol{\sigma} \cdot \langle \Psi^B | \hat{\mathbf{j}} | \Psi^A \rangle$$
$$= -\sum_{i=1}^{N} \int_0^T dt \int_S d\boldsymbol{\sigma} \cdot \langle \varphi_i^B | \hat{\mathbf{j}}_i | \varphi_i^A \rangle \quad (16)$$

of the single-particle, gauge-invariant, current-density operator

$$\hat{\mathbf{j}}_i(\mathbf{r}) = \frac{1}{2\imath} \left[\left(\nabla_i - \imath \frac{\mathbf{A}}{c} \right) \delta(\mathbf{r} - \mathbf{r}_i) + \delta(\mathbf{r} - \mathbf{r}_i) \left(\nabla_i - \imath \frac{\mathbf{A}}{c} \right) \right], \quad (17)$$

evaluated over $\Psi_A(\mathbf{r}; t)$ and $\Psi_B(\mathbf{r}; t)$ or the orbitals which they are composed of. We then replace the bra in equation (16) and insert the expansion equation (6) in Volkov states

$$N_{\text{esc}} = -\sum_{i=1}^{N} \int_0^T dt \int_S d\boldsymbol{\sigma} \cdot \int d^3k \left(b_i^*(\mathbf{k}) \mathbf{J}_{\mathbf{k}}^{(i)} \right) \quad (18)$$

with $\mathbf{J}_{\mathbf{k}}^{(i)} \equiv \langle \chi_{\mathbf{k}} | \hat{\mathbf{j}}_i | \varphi_i^A \rangle$. Since the choice of the subscript A and B in the brakets of equation (16) is arbitrary, we can equivalently choose the opposite order and obtain that N_{esc} is also equal to equation (18) complex conjugated. Comparing equations (10) with (18) and its complex conjugated for each single orbital yields the final expression for the spectral amplitude

$$b_i(\mathbf{k}) = -\int_0^T dt \int_S d\boldsymbol{\sigma} \cdot \mathbf{J}_{\mathbf{k}}^{(i)}, \quad (19)$$

in terms of the Volkov projected single-particle current density $\mathbf{J}_{\mathbf{k}}^{(i)}$. The momentum probability distribution $P(\mathbf{k})$ can then be obtained from equation (11) by summing up $|b_i(\mathbf{k})|^2$ over the orbital index i.

From equation (19) it is apparent that the extension to TDDFT is straightforward. In practical implementations

one needs to calculate $\mathbf{J}_\mathbf{k}^{(i)}$ for a given set of $\mathbf{k}$ and accumulate its flux integral over time. To this end, one needs only to keep track of the KS orbitals $\varphi_i^A(\mathbf{r}; t)$ and their gradients over S while the Volkov waves (and their gradients) are analytical. In principle, provided S is positioned far enough from the system, there is no restriction to the choice of its shape. However, we found that a spherical surface is advantageous from the numerical standpoint as it allows to expand the Volkov waves in spherical harmonics to decouple $\mathbf{k}$ and $\mathbf{r}$. This in turn, requires to truncate the integrals over the sphere up to a given maximum angular momentum $L_{\max}$ and thus introduces an additional parameter to converge (see Appendix A). In practice, we observed that $L_{\max} \approx 100$ is enough for a large class of problems involving moderately strong fields ($I \lesssim 10^{14}$ W/cm^2).

Finally, we mention that a variant of the sampling point method can be derived by truncating the surface integral in equation (19) to a single point (see Appendix B). This leads to an alternative expression similar to the one for PA-SPM. In our tests, however, we found that this variant did not present any significant improvement over PA-SPM and therefore we did not develop it further.

2.4 Mask method

Similar in philosophy to t–SURFF, the mask method (MM) is derived under the same assumption on the ionization process. We here recall the salient traits and remind the reader to references [53,56,57] for further details.

As discussed in Section 2.1, in the long-time limit of an ionization process, we can assume that the electronic density and hence the wavefunction splits into two spatially separated parts. A practical way to implement this splitting for a generic time t is to use a mask function $M(\mathbf{r})$ on each KS orbital as follows

$$\varphi_i(\mathbf{r}; t) = M(\mathbf{r})\varphi_i(\mathbf{r}; t) + [1 - M(\mathbf{r})]\varphi_i(\mathbf{r}; t)$$
$$= \varphi_i^A(\mathbf{r}; t) + \varphi_i^B(\mathbf{r}; t) , \qquad (20)$$

where $M(\mathbf{r})$ is a continuous function equal to 1 in the inner part of A and that smoothly decays to 0 in B.

Using the the mask we can formally write the solution of the TDKS equations in the whole space as a set of coupled equations,

$$\begin{cases} |\Psi^A(t')\rangle = \hat{M}\hat{U}(t', t)\left[|\Psi^A(t)\rangle + |\Psi^B(t)\rangle\right] \\ |\Psi^B(t')\rangle = [1 - \hat{M}]\hat{U}(t', t)\left[|\Psi^A(t)\rangle + |\Psi^B(t)\rangle\right] , \end{cases} \qquad (21)$$

using the time evolution operator

$$\hat{U}(t', t) = \exp\left\{-i \int_t^{t'} \hat{H}(\tau)d\tau\right\} , \qquad (22)$$

with the time-boundary condition $|\Psi^B(t = 0)\rangle = 0$ and with a mask operator defined as $\hat{M} = \sum_{i=1} M(\mathbf{r}_i)\delta(\mathbf{r}_i - \mathbf{r}_i')$.

Owing to the asymptotic condition equation (4) on the Hamiltonian, $|\Psi^B(t)\rangle$ evolves under the action of $\hat{H}_v$, and we indicate with $U_v(t', t)$ the associated evolution operator. Since $\hat{H}_v$ is diagonal in momentum and $\hat{H}_{\mathrm{KS}}$ is almost local in real space, we can write the equation of motion in a mixed real and momentum space representation. In this representation we can integrate equation (21) by recursively applying the discrete time evolution operator $\hat{U}(\Delta t) \equiv \hat{U}(t + \Delta t, t)$ as follows

$$\begin{cases} \langle\mathbf{r}|\Psi^A(t + \Delta t)\rangle = \langle\mathbf{r}|\hat{M}\hat{U}(\Delta t)|\Psi^A(t)\rangle \\ \qquad\qquad + \langle\mathbf{r}|\hat{M}\hat{U}_v(\Delta t)|\Psi^B(t)\rangle \\ \langle\chi_\mathbf{k}|\Psi^B(t + \Delta t)\rangle = \langle\chi_\mathbf{k}|[1 - \hat{M}]\hat{U}(\Delta t)|\Psi^A(t)\rangle \\ \qquad\qquad + \langle\chi_\mathbf{k}|[1 - \hat{M}]\hat{U}_v(\Delta t)|\Psi^B(t)\rangle, \end{cases} \qquad (23)$$

with the initial condition $\langle\chi_\mathbf{k}|\Psi^B(t = 0)\rangle = 0$. These equations can be written in a closed form for $\langle\mathbf{r}|\Psi^A(t)\rangle$ and $\langle\chi_\mathbf{k}|\Psi^B(t)\rangle$, by including the following set of equations, here explicitly expanded for each KS orbital

$$\begin{cases} \langle\mathbf{r}|\hat{M}\hat{U}(\Delta t)|\varphi_i^A(t)\rangle = M(\mathbf{r})\langle\mathbf{r}|\hat{U}(\Delta t)|\varphi_i^A(t)\rangle \\ \langle\mathbf{r}|\hat{M}\hat{U}_v(\Delta t)|\varphi_i^B(t)\rangle = M(\mathbf{r}) \int \langle\mathbf{r}|\chi_\mathbf{k}\rangle\langle\chi_\mathbf{k}|\varphi_i^B(t)\rangle d^3k \\ \langle\chi_\mathbf{k}|[1 - \hat{M}]\hat{U}(\Delta t)|\varphi_i^A(t)\rangle \\ \quad = \int \langle\chi_\mathbf{k}|\mathbf{r}\rangle[1 - M(\mathbf{r})]\langle\mathbf{r}|\hat{U}(\Delta t)|\varphi_i^A(t)\rangle d^3r \\ \langle\chi_\mathbf{k}|[1 - \hat{M}]\hat{U}_v(\Delta t)|\varphi_i^B(t)\rangle \\ \quad = \langle\chi_\mathbf{k}|\varphi_i^B(t)\rangle - \int \langle\chi_\mathbf{k}|\mathbf{r}\rangle\langle\mathbf{r}|\hat{M}\hat{U}_v(\Delta t)|\varphi_i^B(t)\rangle d^3r. \end{cases} \qquad (24)$$

Once equations (23) and (24) are propagated up to time T, the momentum distribution is straightforwardly obtained by summing up the square modulus of the KS orbitals as in equation (11), namely: $P(\mathbf{k}) = \sum_{i=1}^N |\langle\chi_\mathbf{k}|\varphi_i^B(T)\rangle|^2$. Unlike the approaches described in the previous sections, since equations (23) and (24) include the boundary conditions for the wavefunctions in A and B, there is no need for additional absorbing boundaries.

In a numerical implementation the evaluations of the integrals in equation (24) must undergo some level of discretization. In particular, substituting Fourier integrals with Fourier series introduces unwanted periodic boundaries conditions that reintroduce ionized wavepackets into the simulation box and eventually lead to instability (for details see the appendix of Ref. [53]).

A stabler scheme can be obtained by simplifying equation (24) under the assumption that the electron flow is only outward from A. In this case we can omit the term responsible for the introduction of charge from B, and obtain the modified set of equations

$$\begin{cases} \langle\mathbf{r}|\hat{M}\hat{U}(\Delta t)|\varphi_i^A(t)\rangle = M(\mathbf{r})\langle\mathbf{r}|\hat{U}(\Delta t)|\varphi_i^A(t)\rangle \\ \langle\mathbf{r}|\hat{M}\hat{U}_v(\Delta t)|\varphi_i^B(t)\rangle = 0 \\ \langle\chi_\mathbf{k}|[1 - \hat{M}]\hat{U}(\Delta t)|\varphi_i^A(t)\rangle \\ \quad = \int \langle\chi_\mathbf{k}|\mathbf{r}\rangle[1 - M(\mathbf{r})]\langle\mathbf{r}|\hat{U}(\Delta t)|\varphi_i^A(t)\rangle d^3r \\ \langle\chi_\mathbf{k}|[1 - \hat{M}]\hat{U}_v(\Delta t)|\varphi_i^B(t)\rangle = \langle\chi_\mathbf{k}|\varphi_i^B(t)\rangle. \end{cases} \qquad (25)$$

Together with equation (23) it defines a modified scheme completely equivalent to the previous one in the limit where r_S is big enough to justify the outgoing flow condition. We note that, compared to equation (24), the first two equations in equation (25) governing the evolution of the real-space components of the wavefunction in A, are no longer connected with the momentum-space ones. For this reason the propagation is thus equivalent to a time propagation with a mask function absorber that can introduce spurious reflections at the boundaries. Such reflections can, in principle, be reduced by using the most appropriate mask function absorber or a complex absorbing potential casted in the form of a mask function [63]. In the energy range where the mask function absorbs well, it is possible to carry out stable simulations for long times.

3 Examples

In the following, we illustrate the above mentioned approaches with a few examples. Unless otherwise specified, we use TDDFT at the level of the time-dependent (adiabatic) local-density approximation (ALDA) [64], augmented by an average-density self-interaction correction (SIC) [65] which corrects the tail of the Coulomb potential and yields an accurate ionization potential. Furthermore, in order to prevent artificial reflections at the borders of the simulation box we employ absorbing boundary conditions. In all the simulations the ions were clamped to their equilibrium positions.

All numerical calculations were performed with the real-time, real-space TDDFT code OCTOPUS freely available under the GNU public license [66,67].

3.1 Hydrogen atom

We here present a comparison of all the methods discussed in this paper. To this end, we choose as a benchmark test the case of above-threshold ionization (ATI) in an hydrogen atom. Clearly, there is no need to use TDDFT for a one-electron system, and our interest here is focused to assess the numerical performance and the accuracy of the different methods. For this reason the simulations were carried out at the level of single-particle TDSE. Specifically, we choose laser parameters such that our results can be directly compared to reference [68].

We choose a Cartesian grid of spherical shape with radius $r_{box} = 90$ a.u. including an outer shell of width 40 a.u. with a complex absorbing potential of height $\eta = -0.2$ [63]. We employ a pulse of $N_c = 20$ cycles, linearly polarized along the z-axis with wavelength $\lambda = 800$ nm ($\omega = 1.55$ eV), and intensity $I = 5 \times 10^{13}$ W/cm^2 (quiver amplitude $x_p = 11$ a.u.). Photoelectrons are collected until shortly after the pulse, where the total ionization amounts to $N_{esc} \sim 10^{-3}$. The surface points for the t–SURFF method and the sampling points for the SPM are both located on a sphere of radius $r_S = 50$ a.u. directly in front of the absorbing zone. The flux is evaluated with the expansion in spherical harmonics, equation (A.1), up
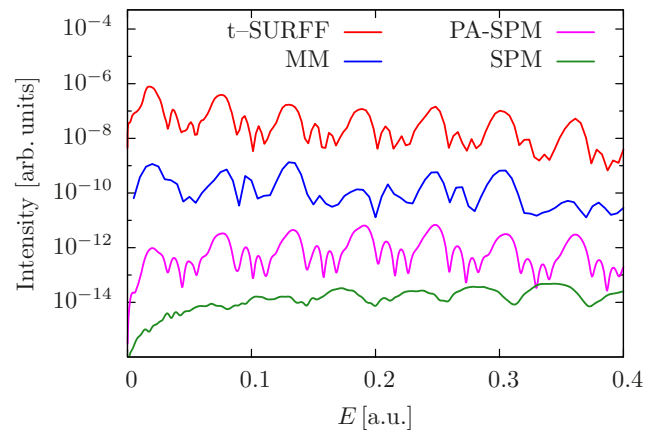

Fig. 2. Calculated photoelectron spectra of hydrogen exposed to a 20-optical-cycle laser pulse with a peak intensity of $I = 5 \times 10^{13}$ W/cm^2 and a frequency of $\omega = 0.057$ a.u., obtained with the t–SURFF, mask (MM), and sampling point methods (SPM and PA-SPM).

to a maximum angular momentum $L_{max} = 20$. The data of the MM is extracted from reference [53] where a box of radius $r_{box} = 60$ a.u. and a mask absorber of width 10 a.u. was used.

Figure 2 shows the total spectra obtained with the three different methods (the offsets are artificial for plotting reasons). Apart from the SPM, all methods compare quite well and display a series of ATI peaks separated by the photon energy $\omega = 0.057$ a.u. The differences between t–SURFF and MM originate from the different resolutions in **k**-space, the different box sizes and width of the mask absorber. In contrast, the SPM presents a featureless background for low-energies which, as the energy increases, transforms into a series of peaks roughly spaced by ω, but with the wrong onset. For this reason, we conclude that the SPM is not suitable for laser excitations in this regime ($\gamma = 1.5$).

The different quality of the results can be better assessed from the angle-resolved spectra. Figure 3 displays high-resolution density plots of the spectra as a function of the kinetic energy E and the angle ϑ measured with respect to the laser polarization axis, obtained with t–SURFF (left), MM (middle), and PA-SPM (right).

The ATI peaks unfold into rings with a number of stripes equal to the angular momentum quantum number of the dominant partial wave in the final state plus one [69]. The low-energy region shows a peculiar nodal pattern which is induced by the long-range Coulomb potential. The pattern for the t–SURFF method compares very well with the MM and with similar calculations in the literature [68]. This demonstrates that t–SURFF is indeed a reliable tool to calculate photoelectron energy-angular distributions in this regime.

Comparing t–SURFF method and MM to PA-SPM, we observe significant differences. While the emission is preferentially along the laser polarization in all cases, PA-SPM underestimates the emission in other directions. In particular, it hardly reproduces the stripes perpendicular
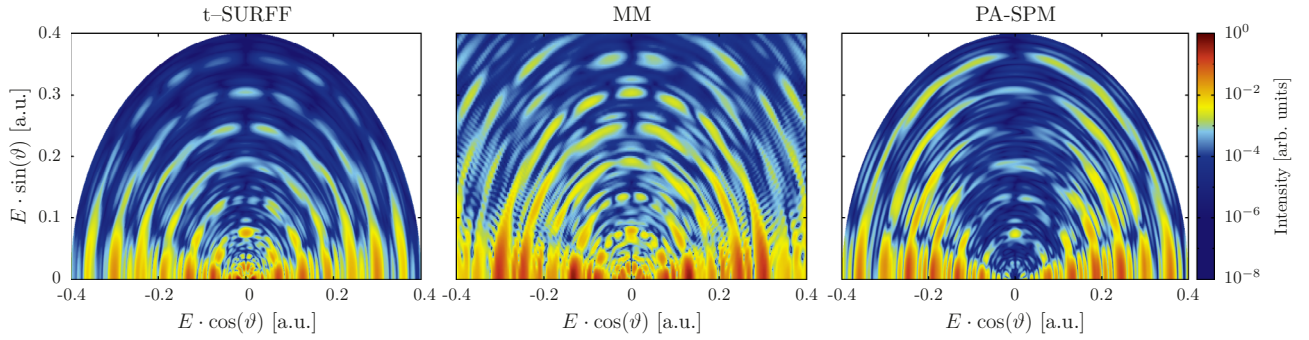
Fig. 3. Calculated photoelectron energy-angular distributions of hydrogen exposed to a 20-optical-cycle laser pulse with a peak intensity of $I = 5 \times 10^{13}$ W/cm^2 and a frequency of $\omega = 0.057$ a.u., obtained with the surface flux (left panel), mask (middle panel), and (phase-augmented) sampling point methods (right panel).

to the laser polarization and the low-energy region which is sensitive to the tail of the Coulomb potential. This failure suggests that the contribution of electrons with momentum not parallel to $\mathbf{r}_S$ neglected by PA-SPM is crucial to form these interference patterns. Therefore, we can conclude that only t–SURFF and MM can be recommended for mid- to strong-field regimes and that all variants of SPM should be avoided. Due to the different box sizes used for t–SURFF and MM, we observe small differences at low kinetic energies between these two methods. Finally, we mention that the single-point approximation of the t–SURFF method (see Appendix B) yields results (not shown) which are in line with those obtained with PA-SPM.

3.2 C$_{60}$ fullerene

Compared to the previous section, we here tackle the more challenging problem in the rescattering regime ($\gamma < 1$) where the use of TDDFT is mandatory. Following reference [70], we consider the fullerene C$_{60}$ exposed to a strong laser pulse, linearly polarized along the z-axis with frequency $\omega = 1.36$ eV, intensity $I = 10^{14}$ W/cm^2, and pulse length $T_{\mathrm{pulse}} = 24$ fs. In reference [70] the positively charged ionic background of the molecule was approximated by a jellium shell and calculations where performed in cylindrical coordinates. As already mentioned in the reference, this model suffers from the fact that returning electrons collide with a jellium well instead of a carbon ion which eventually leads to an underestimation of high-energy electrons. This is a limitation since the angular pattern of rescattered electrons is actually influenced by the interatomic distances as it results from the interference of waves scattering from different ionic centers [71,72]. This is crucial, for instance, for laser-induced electron diffraction [11,12]. Therefore, we choose a three dimensional description which includes the ionic background by modeling each atom with a pseudo-potential [73]. In what follows we consider only a single orientation of the molecule relative to the laser polarization.

t–SURFF allows for computational boxes of the order of the free electron quiver amplitude which for our laser
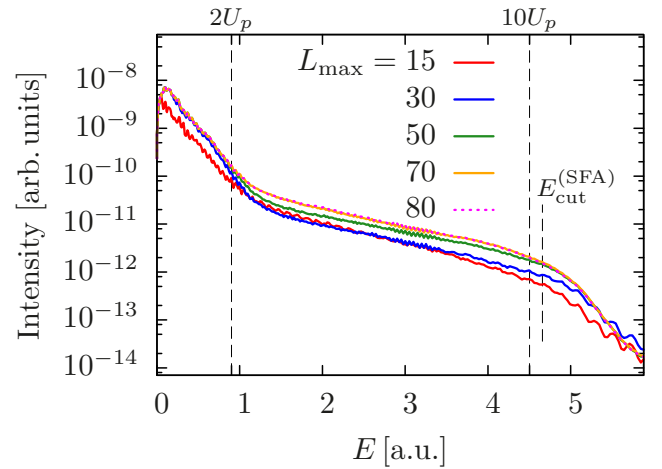

Fig. 4. Calculated photoelectron spectra of C$_{60}$ exposed to a fs pulse with a peak intensity of $I = 1.6 \times 10^{14}$ W/cm^2 and a frequency of $\omega = 0.05$ a.u., obtained for different cut-offs L_{max} in the expansion in spherical harmonics equation (A.1).

is $x_p = 27$ a.u. Here we used $r_{\mathrm{box}} = 70$ a.u. with the surface being located at $r_S = 50$ a.u. in front of a complex absorbing potential of width 20 a.u. and height $\eta = -1.0$. This allows to absorb electrons with kinetic energies from 1 eV to several hundreds of eV. Because of the numerical generation of spherical harmonics, a crucial parameter of the t–SURFF implementation is the angular momentum cut-off L_{max} at which convergence of PES and PAD is reached. Figure 4 shows the obtained spectra for different L_{max} where all the other parameters are brought to convergence. From the figure it is clear that convergence is obtained first for the direct electrons ($E < 2U_p$) at $L_{\mathrm{max}} \sim 30$, and only later, for much higher $L_{\mathrm{max}} \sim 80$, in the plateau region. Nevertheless, all spectra show a large plateau in the range of $E = 30$–125 eV up to the cut-off located at around $E_{\mathrm{cut}}^{(\mathrm{SFA})} = 10.007 U_p + 0.538 E_{\mathrm{IP}}$. ATI peaks can be identified in the direct region with a spacing of the laser frequency ω.

Angular-resolved quantities are displayed in Figure 5 ($L_{\mathrm{max}} = 80$). The angles ϑ and φ are measured with respect to the laser polarization axis (see Fig. 5a). The left
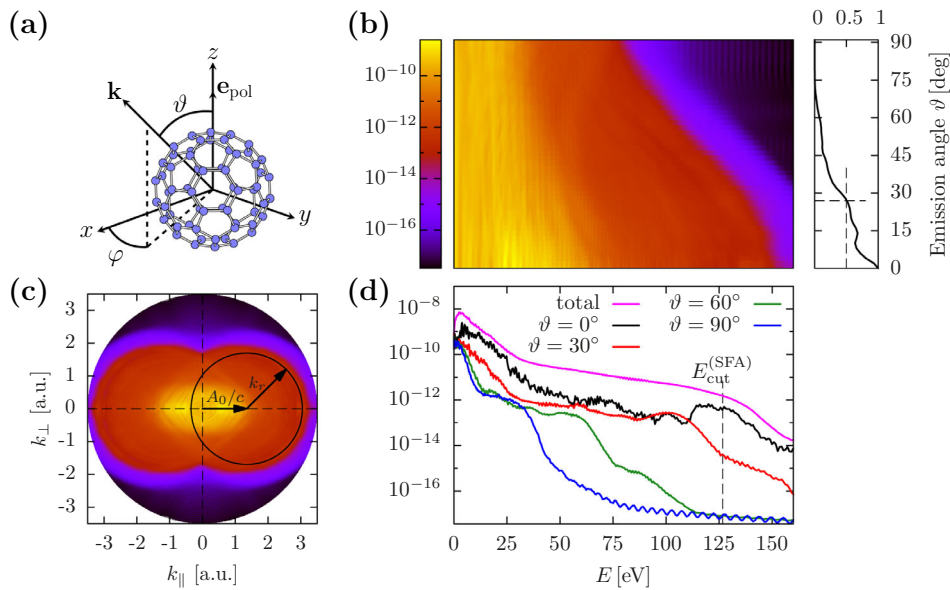
Fig. 5. (a) Geometry of C_{60} fullerene and angles (ϑ, φ) of the outgoing electrons measured with respect to the laser polarization axis (along the z-axis). (b) Color map of calculated angle-resolved photoelectron spectrum of C_{60} as a function of the kinetic energy E and emission angle ϑ, in logarithmic scale. The full three-dimensional momentum distribution was averaged over the angle φ. The right part of (b) shows the PAD obtained from the integration of the angular-resolved PES over the high-energy range of 50–160 eV, normalized to 1 at $0°$. The laser pulse parameters are: $\omega = 1.36$ eV, $T_{pulse} = 24$ fs, $I = 1.6 \times 10^{14}$ W/cm^2. (c) Similar to (b), but as a function of the momenta $k_{\parallel}$ and $k_{\perp}$ parallel and perpendicular to the laser polarization, respectively. (d) Photoelectron spectra for different emission angles ϑ and total PES (in logarithmic scale).

part of Figure 5b shows the full angular-resolved PES averaged over the angle φ, while in the right part we find the PAD obtained from an integration of the angular-resolved PES over the high-energy range of 50–160 eV. As one can see, in this energy range, almost all photo-electrons are emitted with an angle $\vartheta \leq 45°$, i.e., in a cone in forward-backward direction. This in contrast to the jellium model, where the integrated PAD is strongly peaked around $\vartheta = 0°$, we get a larger portion of electrons scattered sidewards. This confirms that the PAD of rescattered electrons is highly sensible to the ionic structure of the target.

Figure 5c displays the momentum distribution $P(\mathbf{k})$ as a function of the momenta $k_{\parallel}$ and $k_{\perp}$ parallel and perpendicular to the laser polarization axis, respectively. The angular-resolved PES is now decomposed by two circles of maximum radii $k_r \approx 1.26 A_0$ which are shifted by $\pm A_0/c$ with respect to the origin. This specific shape is the result of the rescattering process and characteristic of the LIED regime. LIED features can be interpreted with the semianalytical models provided by the quantitative rescattering theory. According to the quantitative rescattering theory [71,72,74], photoelectrons are released by tunnel ionization with an initial velocity of near zero. They then quiver in the laser field before returning back towards the target ion with incident momentum $\mathbf{k}_0$ where they scatter elastically in all directions with scattered momentum $\mathbf{k}_r$ ($|\mathbf{k}_r| = |\mathbf{k}_0|$). The maximum kinetic energy that quiver electrons can gain in the laser field corresponds to $k_r^2/2 = 3.2 U_p = 3.2/4 \cdot A_0^2$, and since the elastic collision occurs in the laser field, photoelectrons gain an addi-

tional momentum $\mathbf{A}(t_r)/c$ from the field at the recollision time t_r. The calculated PAD in Figure 5c fits well with this model. The elastic scattering occurs in all directions. Thus, for a realistic simulation of strong-field ionization it is necessary to use an atomistic model which appropriately describes the rescattering process.

Figure 5d finally shows photoelectron spectra for different emission angles ϑ. Electrons with highest kinetic energies are emitted exclusively along the laser polarization axis, as can be seen at the line for $\vartheta = 0°$. The cut-off is most clearly seen in the total spectrum and fits well with the theoretical prediction $E_{cut}^{(SFA)}$. Spectra of electrons that are emitted sidewards, also exhibit cut-offs, but with values smaller than $E_{cut}^{(SFA)}$.

3.3 Organic molecules

In this section, we move from the strong-field regime to the linear one where the laser intensity is weak, still the photon fluence is large enough to justify the use of a classical description for the electromagnetic field.

In this regime, electrons need to absorb only one photon to ionize. Much like in the photoelectric effect, electrons ejected in this regime carry information about the energy level of their parent system encoded in the kinetic energy spectrum. The spectrum is composed of a series of peaks positioned at kinetic energies $E_i = \omega - E_{IP}^{(i)}$ where $E_{IP}^{(i)}$ is the ionization potential of the ith state of the system. This fact can be easily derived from time-dependent perturbation theory using Fermi's golden rule
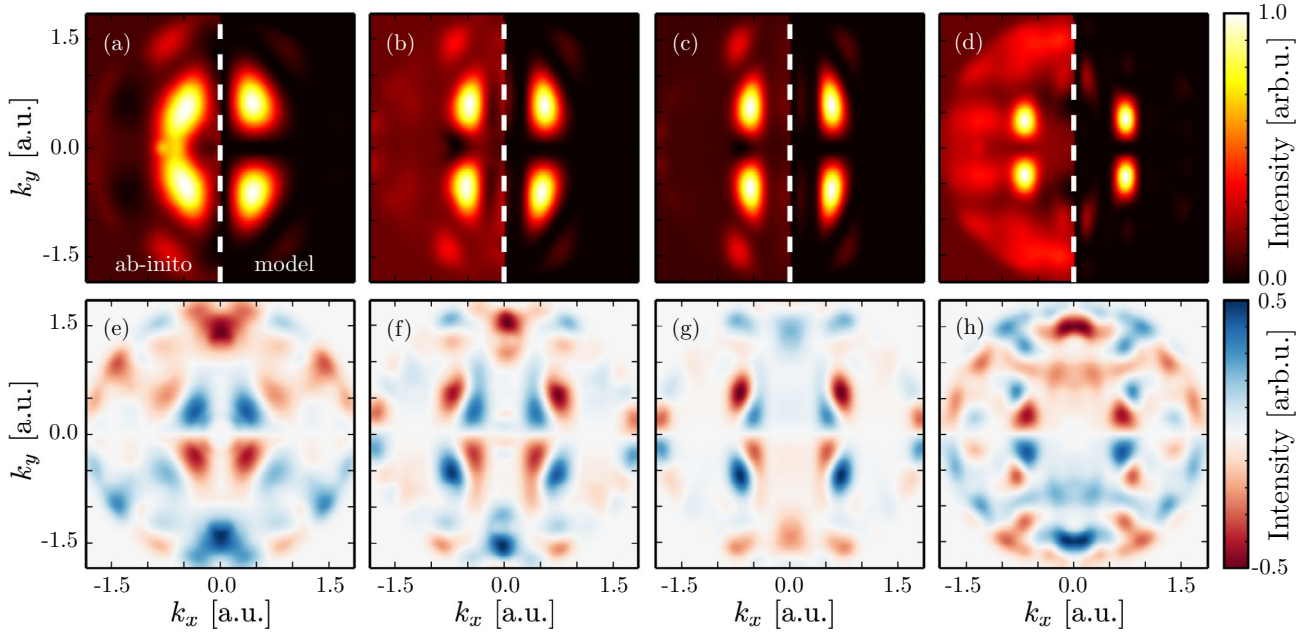
Fig. 6. PADs and PECDs energy cuts for a selection of organic molecules. From left to right in each column we report results for a different molecule: naphtalene (a,e), anthracene (b,f), tetracene (c,g) , and PTCDA (d,h). In the top row PADs are obtained using an unpolarized field (see Eq. (28)), with $\omega = 54.4$ eV, $T_{\text{pulse}} = 9$ fs, and $I = 10^8$ W/cm^2. For all the molecules we oriented the axis such that the x (y) axis is along the longest (shortest) molecular axis while the z axis is perpendicular to the plane of the molecule. Each panel is split in two: in the left part we plot the PAD obtained by the ab-initio simulation using the mask method evaluated on the energy shell corresponding to electrons associated with the HOMO (see text), on the right we plot the Fourier transform of the HOMO orbital evaluated on the same energy shell. In the bottom row we show PECD maps resulting by subtracting the PADs obtained with left and right circularly polarized pulses. The laser has the same parameters as the one used for the top row but circularly polarized on the z-y plane.

which, apart from an inessential scaling factor, reads

$$P(\mathbf{k}) \propto \sum_i |\langle \Psi_f(\mathbf{k})|\mathbf{A} \cdot \hat{\mathbf{p}}|\Psi_i\rangle|^2 \, \delta(E_f - E_i - \omega). \quad (26)$$

This equation describes the probability to excite an electron from an initial state $|\Psi_i\rangle$ to $|\Psi_f\rangle$ separated by $E_{\text{IP}}^{(i)} = E_f - E_i$ using an external field coupled with the dipole matrix element $\mathbf{A} \cdot \hat{\mathbf{p}}$ with $\hat{\mathbf{p}}$ being the momentum operator.

Using equation (26) as a starting point in reference [75] it was first shown that photoelectrons carry also information about the orbitals from which they originate. This information is encoded in the PAD, and can be isolated making the assumption that the final state is a plane wave $|\Psi_f(\mathbf{k})\rangle \approx |\mathbf{k}\rangle$, and that the initial state can be decomposed into separated orbitals $|\varphi_i\rangle$. Under these assumptions, and restricting to energies E_i infinitesimally close to $|\varphi_i\rangle$, equation (26) becomes

$$P(\mathbf{k}) \propto |\langle \mathbf{k}|\mathbf{A} \cdot \hat{\mathbf{p}}|\varphi_i\rangle|^2 = |\mathbf{A} \cdot \mathbf{k}|^2|\tilde{\varphi}_i(\mathbf{k})|^2, \quad (27)$$

where $\mathbf{k}$ is constrained to a spherical energy shell $E_i = \mathbf{k}^2/2 = \omega - E_{\text{IP}}^{(i)}$ and where with $|\tilde{\varphi}_i(\mathbf{k})|^2$ we indicate the Fourier transform of the orbital. Thus, apart from a purely geometrical factor $|\mathbf{A} \cdot \mathbf{k}|^2$, the angular distribution of photoelectrons turns out to be proportional to the Fourier transform of the parent orbital. The geometrical factor can be eliminated by summing up the PADs obtained with two perpendicular polarizations, for instance

along x and y,

$$\begin{aligned} P_U(\mathbf{k}) &= P_x(\mathbf{k}) + P_y(\mathbf{k}) \\ &\propto (|Ak_x|^2 + |Ak_y|^2)|\tilde{\varphi}_i(\mathbf{k})|^2 = 2E_i^2 A^2|\tilde{\varphi}_i(\mathbf{k})|^2, \end{aligned} \quad (28)$$

and we obtain a direct connection between the Fourier transform of orbitals and photoelectron data. Combining incoherently PADs obtained with perpendicular polarizations is equivalent to the use of a single unpolarized pulse. For this reason we named $P_U(\mathbf{k})$ the result of the previous equation.

It must be noted that the aforementioned relation is not universal and is supposed to be valid only for a limited set of molecules and orbitals [75]. The class of planar organic molecules satisfy these conditions and is thus well suited to illustrate the concept. To this end, we calculated $P_U(\mathbf{k})$ ab-initio for a selection of organic molecules: naphtalene, anthracene, tetracene, and perylenetetracarboxylic dianhydride (PTCDA). The results are reported in Figures 6a–6d where we used a laser pulse with $\omega = 54.4$ eV, $T_{\text{pulse}} = 9$ fs, and $I = 10^8$ W/cm^2 and cut at the energy shells corresponding to the HOMO for each molecule, namely $E_H = 46.2$, 47.2, 47.8, 46.6 eV, respectively. All the photoelectron calculations were performed using MM.

In each panel we split the figure in two parts and directly compare $P_U(\mathbf{k})$ (on the left) to the Fourier transform of the HOMO orbital $|\tilde{\varphi}_{\text{HOMO}}(\mathbf{k})|^2$ (on the right).

By comparing right and left parts of each panel it is clear that equation (28) well describes each photoelectron distribution. In a first approximation all these molecules exhibit a similar structure and differ mainly by the number of phenyl rings. For this reason it is not surprising that all the PAD look similar except for small features forming close to zero momentum. This can be indeed understood in terms of Fourier transform where the lobes positioned at $k_y = \pm 1$ a.u. can be associated with a dominant pattern well localized in space – the phenyl ring. This base pattern is repeated for an increasing number of times (and in different directions) as we increase the size of the molecule, and this contributes to create small features in the short wavelengths in reciprocal space (large extension in real space).

Once established the validity of equation (28) it is a natural step to attempt a Fourier inversion and reconstruct the orbitals in real space from the photoemission data. This, however, is not possible since $P_U(\mathbf{k})$ provides only information on the square modulus of the Fourier transform and we lack information about its phase. There have been different attempts in the literature to address this problem and to a large extent they reduce to different levels of educated guessing. For instance, in reference [75], the phase was arbitrarily chosen, while in reference [76] it was selected with a self-consistent procedure and in reference [77] it was identified by correlating group-symmetry arguments with photoelectron circular dichroism (PECD).

In what follows we focus on the last approach. To this end, we calculate the PECD maps subtracting the PAD obtained with left (σ_+) and right (σ_-) circularly polarized laser pulses $P_{CD}(\mathbf{k}) = P_+(\mathbf{k}) - P_-(\mathbf{k})$. For the calculations we choose a field polarized on the y-z axis provided that all the molecules are oriented with the longer (shorter) molecular axis on along x (y) and that z is perpendicular to the molecular plane. The results are shown in Figures 6e–6h. Given that none of the molecules in our set have a specific handedness one would expect to see zero dichroism, but clearly the PECD maps in the figure are not. The apparent discrepancy comes from the fact that it is our observation setup that has a defined handedness and therefore we can observe a dichroic effect even on molecules without a specifc handedness [78]. Furthermore, the results for PTCDA in Figures 6d and 6h are in good agreement with the one measured in reference [77], especially considering that the experiment was carried out with molecules deposited on a metallic surface while our calculations are in the vacuum.

We conclude by observing that the final wave approximation we made to derive equation (27), is inconsistent with a non-zero PECD. In fact, for circularly polarized light, equation (27) becomes

$$
\begin{aligned}
P_\pm(\mathbf{k}) &\propto |\langle \mathbf{k}|A\hat{p}_y \pm iA\hat{p}_z|\varphi_i\rangle|^2 \\
&= P_y(\mathbf{k}) + P_z(\mathbf{k}) \pm i(D_y^* D_z - D_y D_z^*)
\end{aligned}
\tag{29}
$$

where $D_{y,z} = \langle \mathbf{k}|A\hat{p}_{y,z}|\varphi_i\rangle$ is the dipole matrix element. The resulting PECD is $P_{CD}(\mathbf{k}) = 4|D_y||D_z|\sin(\angle D_z - \angle D_y)$ and depends on the phase difference between the two dipole matrix elements of y and z. Approximating

the final wavefunction as a plane wave implies that the matrix element $D_{y,z} = Ak_{y,z}\tilde{\varphi}(\mathbf{k})$ has a phase which is independent of the direction y,z and thus $P_{CD}(\mathbf{k}) = 0$. In order to have a non-zero PECD one has to go beyond the single plane wave final state approximation. Going beyond this approximation may also disclose information on the phase intrinsically encoded in the PECD and possibly allow Fourier inversion without the need of additional information on the group symmetry of the molecule. However, interesting, further investigation along this line is beyond the scope of the current paper.

4 Discussion

Among the presented approaches to calculate photoelectron spectra with TDDFT, the sampling point method appears to be the most straightforward one to implement without effecting much the computational time. However, the errors of the SPM may become severe since the quiver motion of the electron in the laser field is described only approximately at the position of the sampling point. This might lead to inaccurate photoelectron spectra in the strong-field regime. To avoid this, one is forced to choose the size of the box such that electron flow and laser field do not overlap at the sampling point. For example, an electron with kinetic energy of 125 eV travels a distance of ≈125 a.u. within one femtosecond. Therefore, one would need to choose box sizes of hundreds of Bohr in order to obtain reliable spectra of systems exposed to laser pulses consisting of only a few cycles. This basically rules out a computationally efficient usage of the SPM in three dimensions for strong fields. With the PA-SPM the situation improves, but still the results can be inaccurate if the photoelectrons have a non-negligible transversal momentum component at the sampling point.

The mask method, in principle, describes the time evolution of independent particles in the analyzed region (for short-range potentials) exactly as it projects the orbitals onto Volkov states which include the correct phase. This avoids the problem of overlapping electron flow and laser field and allows to choose box sizes which only have to accomodate the quiver motion. Moreover, MM also allows electrons to come back from region B. However, Fourier transforms of the single-particle wavefunctions in the absorbing region are involved. Thus, periodic boundaries are automatically imposed and the resolution in kinetic-energy space depends on grid spacing and width of the absorbing zone. Additionally, the implementation of absorbing boundaries has to be done through a mask function, although it also can be cast in terms of an additional imaginary potential in the Schrödinger equation.

The surface flux method can be seen as a combination of SPM and MM rectifying the disadvantages of both methods. In contrast to the SPM, t–SURFF can be properly derived within a TDDFT formalism. Like in the MM, box sizes can be reduced to approximately the range of the electron quiver amplitude as the quiver motion can be described reliably at the position where the spectrum is evaluated (i.e., the surface). On the other hand, the grid

in momentum space can be chosen arbitrarily up to an energy range of $E_{\max} \lesssim \min\{\pi/\Delta t, (\pi/\Delta x)^2/2\}$, where Δt are the time step and Δx the grid spacing used in the numerical computation. The surface is transparent which means that it allows electrons from region A entering region B and vice versa and that it can be combined with any kind of boundary condition. The calculation of the flux includes the plane wave factor $e^{i\mathbf{k}\mathbf{r}}$ and spatial derivatives of the orbitals that need to be evaluated on a closed surface. Therefore, interpolation may be required and the implementation of the t–SURFF method is more involved than in the SPM. However, it can be fully parallelized in grid points and orbitals.

5 Conclusion

In this paper, we exported t–SURFF to TDDFT using a novel derivation in terms of the flux of the current density operator and discussed how the expansion in spherical harmonics in three dimensions can be crucial for an efficient implementation in real space codes. We have additionally presented other theoretical methods for the calculation of photoelectron spectra within TDDFT: the sampling point method (SPM) and the mask method (MM). While SPM and MM were already established in the framework of TDDFT, t–SURFF is new and has been so far employed in conjunction with other theory levels.

We presented a direct comparison of all the three methods. Our benchmark was the simulation of the characteristic photoelectron angular distribution (PAD) of ATI peaks in an hydrogen atom. In our test, t–SURFF emerged as the best method combining the flexibility and light computational cost of the SPM with the accuracy of the MM in excellent agreement with previously published results.

With t–SURFF we investigated electron emission from the C_{60} molecule exposed to an intense IR laser field. To the best of our knowledge this is the first time that a TDDFT atomistic simulation of strong-field ionization of such a large molecule is presented in the literature. The PES can be separated into direct and rescattered parts with a smooth plateau up to a cut-off at around $E_{\mathrm{cut}}^{\mathrm{SFA}} = 10U_p$. The calculated angular distributions can be well explained with the quantitative rescattering theory and exhibit enhanced sidewards scattering which is completely missing in the same simulation with a jellium model. This underlines the relevance of a theoretical description of strong-field phenomena at the atomistic level.

Finally, we discussed the problem of orbital reconstruction from photoemission data. To this end, we performed simulations with both linearly and circularly polarized pulses on different planar organic molecules. We illustrated how the PAD from unpolarized fields is strongly connected with the Fourier transform of the molecular orbital from which the electrons originate and discussed the problem of Fourier inversion to recover the orbital from photoelectron data. We also performed photoelectron circular dichroism (PECD) simulations that are in good agreement with published data. Furthermore, we showed how non-zero PECD is in direct contrast with

perturbation theory models in which the final state is approximated with a single plane wave and discussed how, going beyond this approximation, may constitute a possible venue to systematically recover the phase for orbital reconstruction.

Appendix A

The main complication for a computationally efficient implementation of equation (19) in three dimensions is the plane wave factor $e^{i\mathbf{k}\mathbf{r}}$ in the Volkov state equation (7) as the number of surface points and the $\mathbf{k}$-grid become large. Therefore, we integrate on a sphere with $d^2\sigma = r_S^2\, d\Omega_r$ and expand the plane wave factor in spherical harmonics:

$$
\begin{aligned}
b_i(\mathbf{k}) &= -\frac{r_S^2}{2i} \int dt \int d\Omega_r\, \chi_{\mathbf{k}}^* \left[\nabla_i + i\mathbf{k} - 2i\frac{\mathbf{A}}{c}\right] \varphi_i^A \cdot \mathbf{e}_r \\
&= -\frac{4\pi r_S^2}{2i(2\pi)^{3/2}} \sum_{lm} (-i)^l j_l(kr) Y_{lm}(\Omega_k) \int dt\, e^{i\Phi(\mathbf{k},t)} \\
&\quad \times \left\{ \left(i\mathbf{k} - 2i\frac{\mathbf{A}}{c}\right) \underbrace{\int d\Omega_r\, Y_{lm}^*(\Omega_r)\, \mathbf{e}_r\, \varphi_i^A}_{\mathbf{S}_{lm}^{(1)}(t)} \right. \\
&\quad \left. + \underbrace{\int d\Omega_r\, Y_{lm}^*(\Omega_r)\, \partial_r \varphi_i^A}_{S_{lm}^{(2)}(t)} \right\}.
\end{aligned}
\tag{A.1}
$$

The expansion has the strong advantage that it decouples the surface integrals $\mathbf{S}_{lm}^{(1)}(t)$ and $S_{lm}^{(2)}(t)$ from the $\mathbf{k}$-grid. The integration can be performed efficiently by using the Gaussian quadrature on interpolated Gaussian nodes up to a cutoff angular momentum $L_{\max}$. For a given $L_{\max}$, the number of integration nodes is independent of the size of the computational box.

Appendix B

The connection between t–SURFF and PA-SPM is to skip the surface integral in equation (19) and to consider only a single point, namely the one pointing in $\mathbf{k}$-direction.

In three dimensions, we proceed by replacing $\mathbf{J}_{\mathbf{k}}^{(i)} \rightarrow \mathbf{J}_{\mathbf{k}}^{(i)} \cdot \delta^{(2)}(\Omega_k - \Omega_r)$ and obtain:

$$b_i^{\text{alt}}(\mathbf{k}) = - \int_0^T dt\, \mathbf{J}_{\mathbf{k}}^{(i)}(r, \Omega_k; t) \cdot \mathbf{e}_k$$

$$= -\frac{e^{-\imath kr}}{2\imath(2\pi)^{3/2}} \int dt\, e^{\imath \Phi(\mathbf{k};t)} \left[\nabla_i + \imath \mathbf{k} - 2\imath \frac{\mathbf{A}}{c} \right]$$

$$\times \varphi_i(r, \Omega_k; t) \cdot \mathbf{e}_k.$$

Assuming $\partial_r \tilde{\xi}(r, \Omega_k; \omega) = \sqrt{2\omega}\imath\, \tilde{\xi}(r, \Omega_k; \omega)$ and identifying $k = \sqrt{2\omega}$, we recover (except for a normalization factor and the term accounting for the vector potential) the result from the PA-SPM.

References

1. L.V. Keldysh, Soviet Phys. J. Exp. Theor. Phys. **20**, 1307 (1965)
2. G. Mainfray, G. Manus, Rep. Prog. Phys. **54**, 1333 (1991)
3. P. Agostini, F. Fabre, G. Mainfray, G. Petite, N. Rahman, Phys. Rev. Lett. **42**, 1127 (1979)
4. T. Brabec, F. Krausz, Rev. Mod. Phys. **72**, 545 (2000)
5. P.B. Corkum, Phys. Rev. Lett. **71**, 1994 (1993)
6. K.C. Kulander, K.J. Schafer, K.L. Krause, in *NATO Advanced Study Institute: Series B: Physics*, edited by B. Piraux, A. L'Huillier, K. Rzazewski (Plenum, New York, 1993), p. 95
7. M. Lewenstein, K.C. Kulander, K. Schafer, P. Bucksbaum, Phys. Rev. A **51**, 1495 (1995)
8. F.H.M. Faisal, J. Phys. B **6**, L89 (1973)
9. H.R. Reiss, Phys. Rev. A **22**, 1786 (1980)
10. F. Krausz, M. Ivanov, Rev. Mod. Phys. **81**, 163 (2009)
11. M. Meckel, D. Comtois, D. Zeidler, A. Staudte, D. Pavicic, H.C. Bandulet, H. Pepin, J.C. Kieffer, R. Dorner, D.M. Villeneuve et al., Science **320**, 1478 (2008)
12. C.I. Blaga, J. Xu, A.D. DiChiara, E. Sistrunk, K. Zhang, P. Agostini, T.A. Miller, L.F. DiMauro, C.D. Lin, Nature **483**, 194 (2012)
13. Y. Huismans, A. Rouzee, A. Gijsbertsen, J.H. Jungmann, A.S. Smolkowska, P.S.W.M. Logman, F. Lépine, C. Cauchy, S. Zamith, T. Marchenko et al., Science **331**, 61 (2011)
14. M. Spanner, O. Smirnova, P.B. Corkum, M.Y. Ivanov, J. Phys. B **37**, L243 (2004)
15. P. Rácz, S.E. Irvine, M. Lenner, A. Mitrofanov, A. Baltuška, A.Y. Elezzabi, P. Dombi, Appl. Phys. Lett. **98**, 111116 (2011)
16. P. Dombi, A. Hörl, P. Rácz, I. Márton, A. Trügler, J.R. Krenn, U. Hohenester, Nano Lett. **13**, 674 (2013)
17. T. Fennel, T. Döppner, J. Passig, C. Schaal, J. Tiggesbäumker, K.H. Meiwes-Broer, Phys. Rev. Lett. **98**, 143401 (2007)
18. S. Zherebtsov, T. Fennel, J. Plenge, E. Antonsson, I. Znakovskaya, A. Wirth, O. Herrwerth, F. Süßmann, C. Peltz, I. Ahmad et al., Nat. Phys. **7**, 656 (2011)
19. B. Piglosiewicz, S. Schmidt, D.J. Park, J. Vogelsang, P. Groß, C. Manzoni, P. Farinello, G. Cerullo, C. Lienau, Nat. Photon. **8**, 37 (2013)
20. M. Krüger, M. Schenk, P. Hommelhoff, Nature **475**, 78 (2011)
21. G. Herink, D.R. Solli, M. Gulde, C. Ropers, Nature **483**, 190 (2012)
22. M.R. Bionta, B. Chalopin, J.P. Champeaux, S. Faure, A. Masseboeuf, P. Moretto-Capelle, B. Chatel, J. Mod. Opt. **61**, 833 (2014)
23. H. Bachau, E. Cormier, P. Decleva, J.E. Hansen, F. Martín, Rep. Prog. Phys. **64**, 1815 (2001)
24. F. Catoire, H. Bachau, Phys. Rev. A **85**, 023422 (2012)
25. S. Chelkowski, C. Foisy, A.D. Bandrauk, Phys. Rev. A **57**, 1176 (1998)
26. X.M. Tong, K. Hino, N. Toshima, J. Burgdörfer, J. Phys.: Conf. Ser. **88**, 012047 (2007)
27. P.L. He, N. Takemoto, F. He, Phys. Rev. A **91**, 063413 (2015)
28. Z. Chen, T. Morishita, A.T. Le, M. Wickenhauser, X.M. Tong, C.D. Lin, Phys. Rev. A **74**, 053405 (2006)
29. M. Awasthi, Y.V. Vanne, A. Saenz, A. Castro, P. Decleva, Phys. Rev. A **77**, 1 (2008)
30. S. Petretti, Y.V. Vanne, A. Saenz, A. Castro, P. Decleva, Phys. Rev. Lett. **104**, 2 (2010)
31. L.B. Madsen, M. Plummer, J. Phys. B **31**, 87 (1998)
32. S.I. Chu, D.A. Telnov, Phys. Rep. **390**, 1 (2004)
33. J. Muth-Böhm, A. Becker, F.H.M. Faisal, Phys. Rev. Lett. **85**, 2280 (2000)
34. I. Dreissigacker, M. Lein, Phys. Rev. A **89**, 053406 (2014)
35. G.L. Yudin, M.Y. Ivanov, Phys. Rev. A **63**, 1 (2001)
36. X.M. Tong, Z.X. Zhao, C.D. Lin, Phys. Rev. A **66**, 033402 (2002)
37. K.I. Dimitriou, D.G. Arbó, S. Yoshida, E. Persson, J. Burgdörfer, Phys. Rev. A **70**, 1 (2004)
38. P. Eckle, A.N. Pfeiffer, C. Cirelli, A. Staudte, R. Dörner, H.G. Muller, M. Büttiker, U. Keller, Science **322**, 1525 (2008)
39. M.V. Ammosov, N.B. Delone, V. Krainov, Sov. Phys. J. Exp. Theor. Phys. **64**, 1191 (1986)
40. P. Puschnig, S. Berkebile, A.J. Fleming, G. Koller, K. Emtsev, T. Seyller, J.D. Riley, C. Ambrosch-Draxl, F.P. Netzer, M.G. Ramsey, Science **326**, 702 (2009)
41. W.D. Grobman, Phys. Rev. B **17**, 4573 (1978)
42. D. Toffoli, P. Decleva, J. Chem. Phys. **137**, 134103 (2012)
43. T. Seideman, Ann. Rev. Phys. Chem. **53**, 41 (2002)
44. F.H.M. Faisal, *Theory of Multiphoton Processes* (Plenum Press, New York, 1987)
45. E. Runge, E.K.U. Gross, Phys. Rev. Lett. **52**, 997 (1984)
46. M.A.L. Marques, N.T. Maitra, F.M.S. Nogueira, E.K.U. Gross, A. Rubio, *Fundamentals of Time-Dependent Density Functional Theory* (Springer-Verlag, Berlin, 2012)
47. J.B. Foresman, M. Head-Gordon, J.A. Pople, M.J. Frisch, J. Phys. Chem. **96**, 135 (1992)
48. J. Zanghellini, M. Kitzler, T. Brabec, A. Scrinzi, J. Phys. B **37**, 763 (2004)
49. M. Dauth, T. Körzdörfer, S. Kümmel, J. Ziroff, M. Wiessner, A. Schöll, F. Reinert, M. Arita, K. Shimada, Phys. Rev. Lett. **107**, 193002 (2011)
50. A.H. Larsen, U. De Giovannini, A. Rubio, in *Density-Functional Methods for Excited States* (Springer International Publishing, Cham, 2015), pp. 219–271

51. A. Pohl, P.G. Reinhard, E. Suraud, Phys. Rev. Lett. **84**, 5090 (2000)
52. P.M. Dinh, P. Romaniello, P.G. Reinhard, E. Suraud, Phys. Rev. A **87**, 032514 (2013)
53. U. de Giovannini, D. Varsano, M.A.L. Marques, H. Appel, E.K.U. Gross, A. Rubio, Phys. Rev. A **85**, 62515 (2012)
54. P. Wopperer, P.M. Dinh, P.G. Reinhard, E. Suraud, Phys. Rep. **562**, 1 (2015)
55. G. Wachter, C. Lemell, J. Burgdörfer, J. Phys.: Conf. Ser. **399**, 012010 (2012)
56. U. De Giovannini, G. Brunetto, A. Castro, J. Walkenhorst, A. Rubio, ChemPhysChem **14**, 1363 (2013)
57. A. Crawford-Uranga, U. De Giovannini, D.J. Mowbray, S. Kurth, A. Rubio, J. Phys. B **47**, 124018 (2014)
58. A. Crawford-Uranga, U. De Giovannini, E. Räsänen, M.J.T. Oliveira, D.J. Mowbray, G.M. Nikolopoulos, E.T. Karamatskos, D. Markellos, P. Lambropoulos, S. Kurth et al., Phys. Rev. A **90**, 033412 (2014)
59. L. Tao, A. Scrinzi, New J. Phys. **14**, 013021 (2012)
60. A. Scrinzi, New J. Phys. **14**, 085008 (2012)
61. J. Caillat, J. Zanghellini, M. Kitzler, O. Koch, W. Kreuzer, A. Scrinzi, Phys. Rev. A **71**, 012712 (2005)
62. F. Morales, T. Bredtmann, S. Patchkovskii, arXiv:1606.04566 (2016)
63. U. De Giovannini, A.H. Larsen, A. Rubio, Eur. Phys. J. B **88**, 56 (2015)
64. J.P. Perdew, Y. Wang, Phys. Rev. B **45**, 13244 (1992)
65. C. Legrand, E. Suraud, P.G. Reinhard, J. Phys. B **35**, 1115 (2002)
66. X. Andrade, D. Strubbe, U. De Giovannini, A.H. Larsen, M.J.T. Oliveira, J. Alberdi-Rodriguez, A. Varas, I. Theophilou, N. Helbig, M.J. Verstraete et al., Phys. Chem. Chem. Phys. **17**, 31371 (2015)
67. A. Castro, H. Appel, M. Oliveira, C.A. Rozzi, X. Andrade, F. Lorenzen, M.A.L. Marques, E.K.U. Gross, A. Rubio, Physica Status Solidi B **243**, 2465 (2006)
68. Z. Zhou, S.I. Chu, Phys. Rev. A **83**, 1 (2011)
69. D.G. Arbó, S. Yoshida, E. Persson, K.I. Dimitriou, J. Burgdörfer, Phys. Rev. Lett. **96**, 143003 (2006)
70. C.Z. Gao, P.M. Dinh, P. Klüpfel, C. Meier, P.G. Reinhard, E. Suraud, Phys. Rev. A **93**, 022506 (2016)
71. C.D. Lin, A.T. Le, Z. Chen, T. Morishita, R. Lucchese, J. Phys. B **43**, 122001 (2010)
72. J. Xu, Z. Chen, A.T. Le, C.D. Lin, Phys. Rev. A **82**, 1 (2010)
73. N. Troullier, J.L. Martins, Phys. Rev. B **43**, 1993 (1991)
74. Z. Chen, A.T. Le, T. Morishita, C.D. Lin, Phys. Rev. A **79**, 1 (2009)
75. P. Puschnig, S. Berkebile, A.J. Fleming, G. Koller, K. Emtsev, T. Seyller, J.D. Riley, C. Ambrosch-Draxl, F.P. Netzer, M.G. Ramsey, Science **326**, 702 (2009)
76. D. Lüftner, T. Ules, E.M. Reinisch, G. Koller, S. Soubatch, F.S. Tautz, M.G. Ramsey, P. Puschnig, Proc. Natl. Acad. Sci. USA **111**, 605 (2014)
77. M. Wießner, D. Hauschild, C. Sauer, V. Feyer, A. Schöll, F. Reinert, Nat. Commun. **5**, 4156 (2014)
78. G. Schönhense, Physica Scripta **T31**, 255 (2007)